Morphological Dynamics-based Anomaly Detection towards *In-situ* Layer-wise Certification for Directed Energy Deposition Processes

Mahathir Mohammad Bappy
Department of Industrial and Systems Engineering, Mississippi State University, MS 39762
mmb888@msstate.edu

Chenang Liu
School of Industrial Engineering and Management, Oklahoma State University, OK 74078
chenang.liu@okstate.edu

Linkan Bian
Department of Industrial and Systems Engineering,
Center for Advanced Vehicular Systems, Mississippi State University, MS 39762
bian@ise.msstate.edu

Wenmeng Tian[1]
Department of Industrial and Systems Engineering,
Center for Advanced Vehicular Systems, Mississippi State University, MS 39762
tian@ise.msstate.edu

Abstract

Process uncertainty induced quality issue remains the major challenge that hinders the wider adoption of additive manufacturing (AM). The defects occurred significantly compromise structural integrity and mechanical properties of fabricated parts. Therefore, there is an urgent need in fast, yet reliable AM component certification. Most finite element analysis related methods characterize defects based on the thermo-mechanical relationships, which are computationally inefficient and cannot capture process uncertainty. In addition, there is a growing trend in data-driven approaches on characterizing the empirical relationships between thermal history and

[1] Corresponding author

anomaly occurrences, which focus on modeling on an individual image basis to identify local defects. Despite of their effectiveness in local anomaly detection, these methods are quite cumbersome when applied to layer-wise anomaly detection. This paper proposes a novel in-situ layer-wise anomaly detection method by analyzing the layer-by-layer morphological dynamics of melt pools and heat-affected zones (HAZs). Specifically, the thermal images are firstly preprocessed based on the g-code to assure unified orientation. Subsequently, the melt pool and HAZ are segmented, and the global and morphological transition metrics are developed to characterize the morphological dynamics. New layer-wise features are extracted, and supervised machine learning methods are applied for layer-wise anomaly detection. The proposed method is validated using the directed energy deposition (DED) process, which demonstrates superior performance comparing with the benchmark methods. The average computational time is significantly shorter than the average build time, enabling in-situ layer-wise certification and real-time process control.

Keywords: Additive manufacturing, anomaly detection, certification, directed energy deposition, morphological analysis, thermal history

1. Introduction

The metal-based additive manufacturing (AM) technologies have demonstrated their significant potential by producing fully functional parts with reduced production time and costs for low-volume and high-value complex-shaped components. The AM technologies provide the opportunity to manufacture parts of diverse designs in both nonstandard and remote environments, which is not feasible for conventional manufacturing processes. Moreover, AM is also capable of

reducing the overall time-to-market of new products by accelerating the in-house testing of the designed prototypes prior to first market introduction [1][2]. The directed energy deposition (DED) process is a widely used metal-based AM process with the capacity of product prototyping, production, and component repair. During the fabrication, the feedstock material is deposited while being melted and subsequently solidified on top of the previous layer to gradually form the final geometry [3]. The high uncertainty in the DED process may lead to quality issues in the final parts, including porosity, cracks, and lack of fusion [4]. These issues will significantly compromise the mechanical properties and reliability of the fabricated AM components, hindering broader adoption of DED technologies in various mission-critical applications. Therefore, there is an urgent need in developing reliable certification methods to accelerate the scale up of DED technologies [4], [5].

AM component certification refers to evaluating the conformity of the component during or after the fabrication based on the pre-established standards [6]. In practice, AM component certification activities are essential to assure the trustworthiness and reliability of the AM components, especially for mission-critical applications [7]. To satisfy the needs for certification, various anomaly detection methods can provide critical information for AM component certification, where different inspection techniques can be adopted to identify and characterize the critical flaws (e.g., porosity, and crack) in the fabricated component [8],[9].

In the DED process, the thermal history is capable of characterizing process dynamics to predict material microstructure and its resulting mechanical properties. Various AM process modeling studies focus on characterizing process thermal history. Some approaches characterize the thermal history using finite element models (FEM) [10], [11]. However, they are usually extremely computationally expensive, highly dependent on the design geometry, and very

cumbersome to capture process uncertainty [4]. Additionally, notable advancements of sensor technologies have enabled *in-situ* monitoring and anomaly detection towards component certification for metal-based AM [4], [12], [13]. Most approaches for *in-situ* AM process monitoring are performed through the feature extraction from thermal images [13]–[15]. Alternatively, the layer-wise thermal image series can capture the complete spatiotemporal information in a layer-wise manner, which is more robust for anomaly detection of the fabricated parts. However, in most studies, only local features extracted from individual thermal images are considered, and those approaches cannot be directly applied to layer-wise certification, and the key reasons include: 1) the thermal distribution of different layers varies continuously (i.e., mushroom effect), and thus it is difficult to establish one benchmark distribution for all the layers in one build [4]; 2) given a complicated component, the thermal behavior also varies as a function of the printing path, which needs to be accounted for in the anomaly detection method [16]; and 3) the state-of-the-art approaches are usually purely data-driven and thus do not directly quantify the morphological dynamics of melt pools [17], [18], which often makes their anomaly detection models and results challenging to interpret.

To fill these gaps, a new *in-situ* layer-wise AM anomaly detection method is proposed by characterizing the morphological dynamics of the melt pools and heat affected zones (HAZs) which are segmented based on specific temperature ranges. In this study, the optimal transport problems are leveraged to formulate the morphological dynamics, and a new Wasserstein distance-based transition metric system is developed to characterize the temporal variation in the melt pool and HAZ morphologies, respectively. Subsequently, several new layer-wise key process features are extracted and used for layer-wise anomaly detection, facilitated by a supervised machine learning framework.

The *technical contributions* of this paper are summarized as follows. First, it explicitly establishes a physics-informed formulation of layer-wise melt pool and HAZ morphology dynamics to characterize the stability of thermal history. Second, several novel layer-wise process key features are proposed for the layer-wise anomaly detection of the DED process based on the melt pool and HAZ transition metrics with validated better performance than the state-of-the-art approaches, providing critical information towards AM component certification. The impacts to the research community and industries are two-fold. For the AM quality control area, the newly proposed method opens the new venue of physics-informed data-driven anomaly detection for AM processes, which provides critical information for component-wise certification as well as guiding *in-situ* process control practices for AM quality improvement. For AM industrial practices, reliable layer-wise anomaly detection can significantly reduce the needs for post-manufacturing inspection for AM components certification, and ultimately accelerate the broader adoption of AM technologies in mission-critical applications.

The remainder of the paper is organized as follows. A literature review on the state-of-the-art metal-based AM process anomaly detection techniques is summarized in section 2. The proposed methodology for developing the new melt pool and HAZ transition metrics and their properties, and layer-wise certification are introduced in section 3. In section 4, case studies of fabricating a thin wall and a cylindrical specimen using the DED process are presented, and the performance of the proposed method is compared with the benchmark methods. Finally, section 5 presents the conclusion and potential future research directions.

2. Literature Review

This section briefly summarizes the state-of-the-art methodologies for metal-based AM process anomaly detection. The major metrological technologies used for AM anomaly detection

are firstly summarized. Subsequently, the defect characterization and modeling techniques based upon the data collected using the metrological technologies are summarized. Lastly, the research gaps of machine learning based AM anomaly detection are briefly discussed.

2.1 Metrological Techniques for AM Anomaly Detection

Most data-driven AM anomaly characterization methods heavily rely on data collected from the metrological techniques used. In this section, a comprehensive review and comparison among different metrological techniques used for AM quality assurance and certification is conducted. The respective merits and limitations of the most widely used metrological approaches are briefly summarized in Table 1.

All the metrological techniques can be briefly categorized into two types, *in-situ* and post-manufacturing techniques (as illustrated in Table 1). In cases of *in-situ* sensing technologies, the measurements are taken from the system without interrupting or hampering the AM process. The post-manufacturing inspection technologies, on the other hand, can only be used after the completion of the part fabrication. Therefore, those *in-situ* metrological techniques can be used to develop real-time process monitoring and quality prediction models, and the post-manufacturing approaches can be used to provide the validation for those data-driven models.

Table 1: Comparison of different metrological techniques

Approach	Data Description	Merits	Limitations	Inspection Type
X-ray Computed Topography (XCT)	The XCT generates 3D images of a specimen by combining cross sectional image of the object to represent internal structure non-destructively [19], [20].	• Characterizes internal defects and structure of the object. • Generates 3D voxel geometry based on 2D radial slices [19]	• Time intensive and costly [20]. • Limited size of the inspected parts. • Require high capacity computer data storage [19].	Post-manufacturing
Magnetic Resonance	The MRI captures the cross-sectional	• Performs scanning without radiation.	• Very expensive.	Post-manufacturing

Imaging (MRI)	image of structure [21].	• Suitable for soft structure [21].	• Requires enclosed space due to loud noise [20].	
Ultrasonic Testing (UT)	UT generates phase velocity to measure flaws in the test specimen [22].	• Unhazardous process [20].	• Expensive technique. • Specimen surface needs to be accessible and smooth [22].	Post-manufacturing
Pyrometer	Pyrometer captures in-situ temperature profile as a thermal image [12].	• Non-contact method. • Suitable for thermal hazardous environments [20].	• Noise affects measurement efficiency. • Loss of thermal radiation spectrum [20].	*In-situ*
IR camera	It uses infrared and the visual region to produce image of the object [20].	• Captures thermal information with images [20].	• Range of emissivity and reflection affects accuracy [20].	*In-situ*
High-speed camera	It captures images of high-speed processes [20].	• Very high image capture rate [20].	• Lens distortion and non-alignment of sensor generate erratic image [20].	*In-situ*
3D Scanner	It collects point clouds – a type of high-density data in 3D coordinate systems in a fast and reliable manner [23][24].	• More sensitive to geometric variations of object [23].	• Only captures the morphological information of the scanned object [23].	*In-situ*

2.2 Post-manufacturing Anomaly Characterization

The defect characterization methods, including XCT, MRI, and UT, are widely used for post-manufacturing anomaly characterization of AM parts [3]–[5]. The XCT technique is used in metal-based AM to measure porosity occurrences, their spatial distribution, and severity in the build parts [12], [25]. The XCT data can be analyzed using the Computer Aided Quality (CAQ) technology to trace the porosity orientation in the printed parts [26]. Moreover, the XCT can be analyzed using machine learning tools for automatic segmentation of porosity from the scanned images of metallic

specimens [27]. Compared to other post-manufacturing methods, XCT can provide detailed 3D information even for complex geometries. However, the XCT process usually requires high energy and skilled operators to operate the machine. In addition, the XCT machine is subject to high capital cost, and the inspection process is extremely time consuming [20].

MRI is used to track the overall structure of the AM parts using radio frequency pulses and powerful magnetic field [21]. The MRI systems can produce the cross-sectional images of the structures by capturing magnetic field intensity gradient without ionizing radiation as observed in XCT scans [20], [21]. However, in this approach, a complex shape may need to be tested for multiple times to obtain precise structural information, making it time consuming and complicated in data collection [20].

The UT technology is also primarily used to characterize the internal structure of parts [28]. Basically, the ultrasonic phase velocity is used to characterize the defects like pores and voids in AM parts. In some studies, during experimentation, the samples are printed with a porosity of up to 5-15%, and the output denotes that the measured phase velocity is inversely proportional to porosity [22], [29]. Moreover, the ultrasonic phase velocity can characterize defects and microstructures of AM parts. For example, changing process parameters, like hatch spacing and mechanical properties can affect the defect formation, leading to varying pores numbers, sizes and shapes, which can be captured by the UT technology [22]. As a non-destructive technique, UT measurements can be integrated with other monitoring techniques for developing a comprehensive evaluation system for AM parts. It is very important to maintain standard experimental procedures including voltage gain, pulse repetition frequency, and good surface finish otherwise few degrees of change can deviate important signal information [29].

In summary, although the post-manufacturing approaches generate good information about the internal structure and surface properties of the AM parts, they are extremely high skill demanding, time consuming, and costly in nature [4], [20]. Therefore, it is challenging and usually impractical to extensively apply these post-manufacturing technologies in AM certification. However, the detailed information and superior accuracy of post-manufacturing approaches make them a good choice for providing limited labeling information for supervised and/or semi-supervised learning for *in-situ* AM certification.

2.3 *In-situ* Anomaly Detection and Process Monitoring based on Image Analysis

In-situ monitoring of the AM process can capture the process uncertainty and thus can certify the AM process/part in real time. For *in-situ* AM process monitoring and anomaly detection, multiple data sources of thermal imaging, optical imaging and 3D scanning can be used to capture the process information during the fabrication of AM parts. In this section, the recent works in anomaly detection are categorized based on the sensing technologies used, namely, thermal imaging, video streams, and 3D point cloud.

The thermal characteristics are identified as one of the most informative process signals for the AM process dynamics. During the fabrication of AM parts, the thermal history can be used for process monitoring, microstructural assessment, and mechanical properties prediction [30]. In general, the AM process thermal history is captured as a high-resolution thermal image stream, which are subsequently used for developing data-driven approaches to model process dynamics for anomaly detection [12], [31]–[33]. In the specific case of metal-based AM, major proportion of the published works are conducted with thermal imaging systems, where the machine learning based models are developed for *in-situ* anomaly detection. In some studies, along with the thermal history, the morphological features of the melt pool (e.g., depth, size, and temperature distribution)

are extracted for anomaly detection [11], [12], [14]. Furthermore, instantaneous temperatures, melt pool orientations and aspect ratios are also estimated based on pyrometry observation for defect detection [34]. Besides these, tensor decomposition has been applied to the thermal images for dimension reduction, making it easy to model the process-defect relationship [4]. In addition, deep learning based models are developed to link the layer-wise images and the ground truth XCT data for autonomous anomaly detection and classification [35], [36]. Moreover, unsupervised anomaly detection method based on neural networks is also used for distance-based multivariate anomaly detection [37]. With only a few exceptions of layer-wise modeling proposed by Seifi *et al*. [4] and Esfahani *et al.* [16], most of the existing data-driven approaches focus on process monitoring and anomaly detection only considering individual thermal images, which fails to characterize layer-wise process condition and part quality. However, quantifying the morphological variability of the multiple melt pools within a layer will provide a new process knowledge driven approach for anomaly detection.

Another stream of research utilizes the *in-situ* optical video acquisition technique, which has become more accessible due to the availability of robust machine vision systems integrated with the AM process, enabling highly efficient online anomaly detection and process monitoring [38]–[40]. Using the video as a spatiotemporal data stream, the integrated spatiotemporal decomposition and regression-based modeling is proposed for *in-situ* anomaly detection and monitoring [41]. In addition, this method can be applied to any image-based process monitoring applications where the foreground events are random and sparse, and the anomaly is spatially and temporally correlated. A recursive estimation procedure for real-time implementation of the algorithm is also proposed to handle the challenges of the high dimensionality of the video-image stream. However,

the spatial information of the video streams may not be sufficient to distinguish the anomalous events from other natural foreground [41], [42].

3D point cloud data are used for geometric deviation and surface defect detection of AM parts [23], [43]. The machine learning models can be trained with synthetic 3D point clouds rather than experimental data that can reduce training time and costs associated with many prints for each design [44]. Basically, 3D point clouds are high density data, and used to measure the geometric integrity of the AM products fabricated through a variety of processes. Specifically, dimensional or surface variation induced by miniature process shifts in AM system can be detected and characterized using point cloud based approaches [23]. For instance, the laser-scanned 3D point cloud data are used for identifying dimensional variation in AM parts [45]. Although the points clouds data are more capable of depicting structural information of the printed parts compared to low-dimensional signals, translating the 3D point clouds data into a model is very difficult due to the computational complexity and segmentation precision issues [45], [46].

2.4 Discussion of Research Gaps

This subsection discusses the research gaps in the state-of-the-art machine learning-based anomaly detection methods for anomaly detection of metal-based AM processes.

The machine learning models aim to capture the process-defect relationships to distinguish between anomaly-inducing samples and healthy samples, with various machine learning models being adopted [18], [33]. One group of mostly used machine learning approaches are the deep learning related methods, which include convolutional neural network [47][48][49], long-term recurrent convolutional networks [50], deep belief networks [51], and self-organizing maps [14]. Although these methods demonstrate great success in capturing the patterns to distinguish the anomalies from the healthy samples, they also have some major limitations when being applied to

layer-wise anomaly detection. First, these models need to be trained using a large training dataset, which can be quite costly for layer-wise anomaly detection. Second, most deep learning models demonstrate limited model interpretation since they are usually regarded as black-box models. Third, it is very challenging for the deep learning related methods to incorporate engineering domain knowledge, such as the layer-wise printing trajectory information, in the modeling and anomaly detection.

In addition, various other methods first leverage feature extraction approaches to extract critical process features from the high-dimensional raw process signals, and subsequently apply various machine learning approaches. The low-dimensional features extracted include melt pool geometric features [52], melt pool boundary related morphological characteristics [13], melt pool surface temperature related features [14][53], tensor decomposition based features [4], [12], auto-encoder based features [54] [55], and various summary statistics of the raw signals [56]. Once the features extracted, various machine learning methods, such as support vector machines [4] [13] [32] [57], discriminative models [32] [56], and random forests [58], have been used for anomaly detection. These methods have demonstrated good performance in anomaly detection for individual observations (e.g., single melt pool images). However, they can be quite cumbersome when being applied to layer-wise anomaly detection for the following two main reasons. First, the thermal distribution of different layers in the same build is continuously varying, and thus it is difficult to establish one benchmark distribution for all the layers in one build. Second, given a complicated component, the thermal behavior also varies as a function of the printing path, which needs to be accounted for in the anomaly detection method.

To fill the above-mentioned gaps, the proposed method aims to extract layer-wise process features that can account for the varying thermal distribution due to different layer change as well

as constantly changing printing trajectories. A new *in-situ* layer-wise AM anomaly detection method is proposed by characterizing the morphological dynamics of the melt pools and heat affected zones (HAZs) which are segmented based on specific temperature ranges. Subsequently, the Wasserstein distance (WD)-based morphological transition metric features can be extracted for layer-wise anomaly detection, and a support vector machine based supervised machine learning framework is leveraged for layer-wise anomaly detection.

3. Methodology

In this section, the proposed methodology is introduced. The melt pool and HAZ in the thermal images are firstly segmented, and subsequently the new melt pool/HAZ transition metrics are derived by leveraging the Wasserstein distance to quantify the perturbation in a series of melt pools/HAZs' morphologies. The resulted transition metrics are used to extract critical layer-wise features for anomaly detection towards AM part certification. Finally, the supervised learning method is leveraged for layer-wise anomaly detection based on the labeling information generated by post-manufacturing inspection methods, such as X-ray CT. The overall steps of the proposed methodology are illustrated in Figure 1a, and the data visualization of multiple key steps are shown in Figure 1b-e.

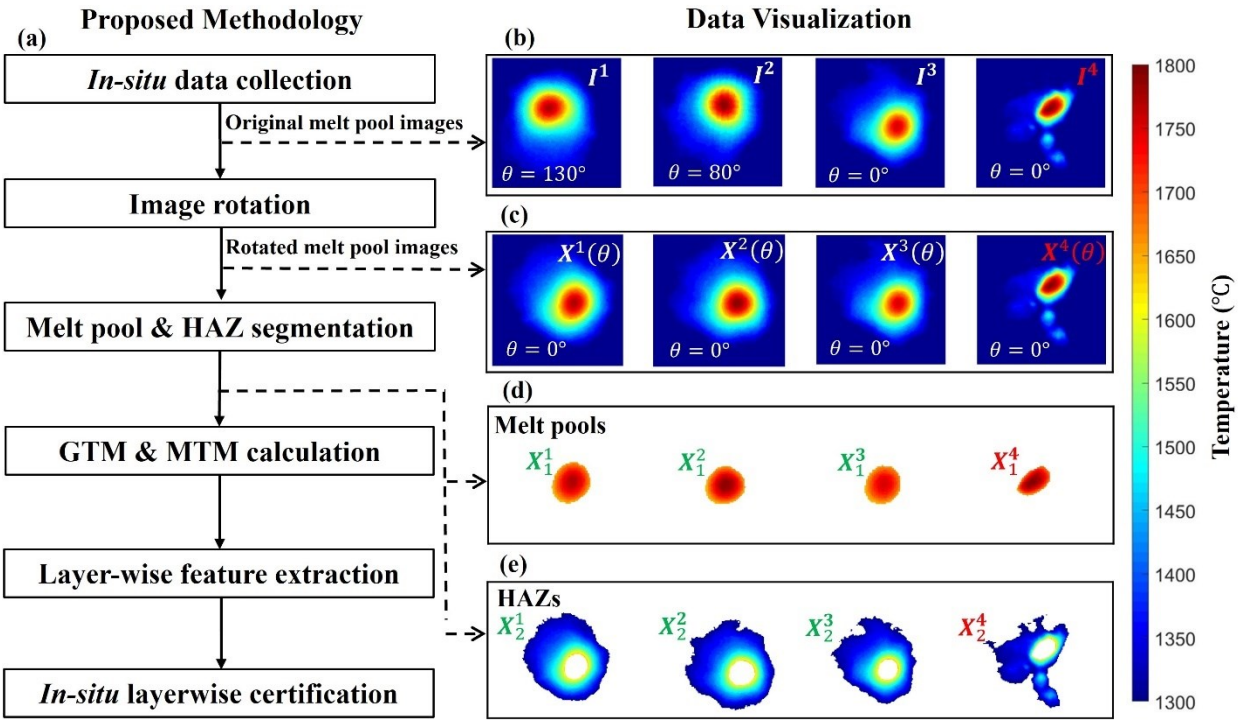

Figure 1: The proposed method of *in-situ* layer-wise anomaly detection by characterizing morphology dynamics of melt pools and HAZs.

3.1 Melt Pool and Heat Affected Zone Identification

The thermal images are captured using a pyrometer camera that consists of a temperature measurement at each pixel within the field of view of the camera. To compress the thermal image data without losing useful information for anomaly detection, the widely used concept of heat affected zones is adopted in this paper together with the melt pool to provide more comprehensive information to characterize the observed temperature distribution. For the sake of clarify, the heat affected zone observed in the thermal image is defined as below.

Definition I: Heat affected zone (HAZ). In each thermal image, the region with temperature readings within a pre-specified temperature range of interests which is lower than the melting temperature (e.g., $\mathcal{R}_2$) of the material is defined as the heat affected zone (HAZ).

The melt pool and HAZ's morphologies are primarily governed by two major factors, i.e., the printing path and the AM process stability. Therefore, to quantify the process stability, the printing

path induced variability needs to be firstly removed from the observed thermal history. During the AM fabrication, the instantaneous melt pool orientation is determined by the instantaneous printing direction, which can be calculated from the printing path in the g-code [16]. Therefore, the image rotation operation is leveraged to align the melt pools with consistent orientation in each layer, as illustrated in Figure 1(c). Let $\mathbf{I}^t \in \mathbb{R}^{r\times c}$ denote the original thermal image collected at time t, which is a matrix with dimension $r \times c$, where r and c are the numbers of rows and columns, respectively. Then, the rotated image can be obtained by Equation (1),

$$\mathbf{X}^t(\theta) = R\left(\mathbf{I}^t, (\theta - \alpha^t)\right) \tag{1}$$

where $\mathbf{X}^t(\theta) \in \mathbb{R}^{r\times c}$ denotes the rotated image and the function R denotes the image rotation operation given the pre-specified target orientation θ. Moreover, α^t represents the theoretical instantaneous orientation of the original melt pool ($\mathbf{I}^t$) that can be obtained from the g-code. Furthermore, it is also noted that the selection of θ may consider the major printing orientation in the specific layer to minimize the rotation operations needed. As a result of the rotation operations, the variability of the aligned thermal images (i.e., $\mathbf{X}^t(\theta)$) is mainly determined by the AM process variability.

Subsequently, the melt pools and HAZs are obtained by segmenting $\mathbf{X}^t(\theta)$ based on the corresponding temperature ranges of interests, as presented in Equation (2).

$$(\mathbf{X}_k^t)_{a,b} = \begin{cases} \left(\mathbf{X}^t(\theta)\right)_{a,b}, & \text{if } \left(\mathbf{X}^t(\theta)\right)_{a,b} \in \mathcal{R}_k \\ 0, & \text{if } \left(\mathbf{X}^t(\theta)\right)_{a,b} \notin \mathcal{R}_k \end{cases}, k = 1,2 \tag{2}$$

where $\mathbf{X}_1^t \in \mathbb{R}^{r\times c}$ denotes melt pool region in which $(\cdot)_{a,b}$ representing the entry at the a-th row and b-th column ($a = 1,2,\dots,r$ and $b = 1,2,\dots,c$) with $\mathcal{R}_1 = [T_m, +\infty)$ and T_m is the melting temperature of the feedstock material. In addition, $\mathbf{X}_2^t \in \mathbb{R}^{r\times c}$ denotes HAZ region with $\mathcal{R}_2 = [T_0, T_m)$.

3.2 Melt Pool and HAZ Transition Metrics and their Properties

A new transition metric system for both melt pools and HAZs is developed by leveraging the Wasserstein distance formulation. The newly developed transition metrics are introduced as below.

Definition II: Global Transition Metric (GTM). The GTM, denoted as $\mathrm{GTM}(\mathbf{X}_k^t, \mathbf{X}_k^{t+1})$, quantifies the global mean transition between consecutive melt pools/HAZs, and can be thus calculated from the absolute difference between the total summation of the two consecutive melt pools/HAZs, i.e., $\mathbf{X}_k^t$ and $\mathbf{X}_k^{t+1}$, as shown in Equation (3),

$$\mathrm{GTM}(\mathbf{X}_k^t, \mathbf{X}_k^{t+1}) = |\mathbf{1}_r^T \mathbf{X}_k^t \mathbf{1}_c - \mathbf{1}_r^T \mathbf{X}_k^{t+1} \mathbf{1}_c| \tag{3}$$

where $\mathbf{1}_v$ represents a $v \times 1$ vector of ones, and thus $\mathbf{1}_r^T \mathbf{X}_k^t \mathbf{1}_c$ equals to the sum of all the entries in $\mathbf{X}_k^t$.

Definition III: Morphological Transition Metric (MTM). The MTM focuses on the instantaneous morphological changes between consecutive melt pools/HAZs. After removing the effect of GTM, the normalized melt pools/HAZs can be generated as show in Equation (4).

$$\mathbf{Z}_k^t = \mathbf{X}_k^t / (\mathbf{1}_r^T \mathbf{X}_k^t \mathbf{1}_c) \tag{4}$$

where $\mathbf{Z}_k^t \in \mathbb{R}^{r \times c}$ denotes the normalized HAZ with k-th temperature range $\mathcal{R}_k$. The normalized melt pools/HAZs are used to develop Wasserstein distance based on the optimal transport formulation. To better illustrate the formulation of the optimal transport problem, the terminologies of weight, flow, and work are defined as below.

Definition IV: Weight. The pixel-wise values in the normalized melt pools/HAZ $\mathbf{Z}_k^t$ are defined as the weight, denoted as $w_{k,i}^t$, where i is the one-dimensional index in matrix $\mathbf{Z}_k^t$ and $i = 1,2, \dots, rc$. In addition, it denotes the normalized temperature value in the melt pools/HAZs.

Definition V: Flow. The flow, denoted as $\boldsymbol{\mathcal{F}}(\mathbf{Z}_k^t, \mathbf{Z}_k^{t+1}) = \left[f_{ij}^{t,t+1}\right]_{rc\times rc}$, represents the pixel-wise weight transport from $\mathbf{Z}_k^t$ to $\mathbf{Z}_k^{t+1}$ to achieve the identical normalized melt pools/HAZs, as illustrated in Figure 2. Here, rc is the total number of pixels in $\mathbf{Z}_k^t$ and $\mathbf{Z}_k^{t+1}$.

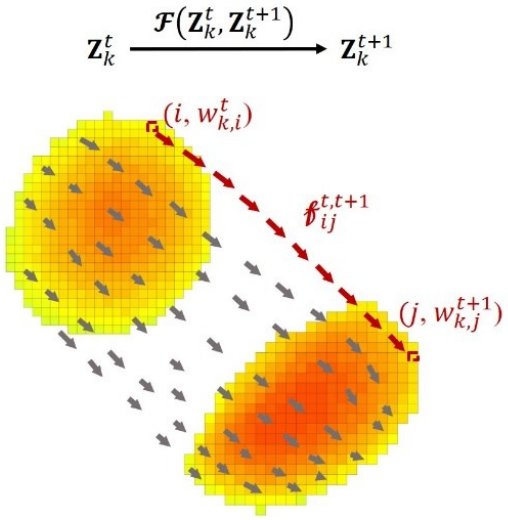

Figure 2: Visualization of flow $\boldsymbol{\mathcal{F}}(\mathbf{Z}_k^t, \mathbf{Z}_k^{t+1})$, with $f_{ij}^{t,t+1}$ denoting the transport from the i-th pixel of $\mathbf{Z}_k^t$ to the j-th pixel of $\mathbf{Z}_k^{t+1}$.

Definition VI: Work. The work resulted from a feasible flow $\boldsymbol{\mathcal{F}}(\mathbf{Z}_k^t, \mathbf{Z}_k^{t+1})$ in matching $\mathbf{Z}_k^t$ and $\mathbf{Z}_k^{t+1}$ is defined as below.

$$\mathrm{Work}\left(\boldsymbol{\mathcal{F}}(\mathbf{Z}_k^t, \mathbf{Z}_k^{t+1})\right) = \mathrm{tr}\left(\mathbf{D}(\mathbf{Z}_k^t, \mathbf{Z}_k^{t+1})^T \boldsymbol{\mathcal{F}}(\mathbf{Z}_k^t, \mathbf{Z}_k^{t+1})\right) \tag{5}$$

where $\mathbf{D}(\mathbf{Z}_k^t, \mathbf{Z}_k^{t+1}) = \left[\left\|\boldsymbol{u}_{k,i}^t - \boldsymbol{u}_{k,j}^{t+1}\right\|\right]_{rc\times rc}$ represents the Euclidean distance matrix between individual pixels in $\mathbf{Z}_k^t$ and $\mathbf{Z}_k^{t+1}$, where $\boldsymbol{u}_{k,i}^t \in \mathbb{R}^{1\times 2}$ represents the 2D coordinates of the i-th pixel in $\mathbf{Z}_k^t$, and $\boldsymbol{u}_{k,j}^{t+1} \in \mathbb{R}^{1\times 2}$ represents the 2D coordinates of the j-th pixel in $\mathbf{Z}_k^{t+1}$ (i and $j = 1, \dots, rc$). For clarification purpose, a simple demonstrative example with two simple HAZs along with the flow and distance matrix between them is presented in Figure 3 to illustrate the definition of different matrices in the computation of work.

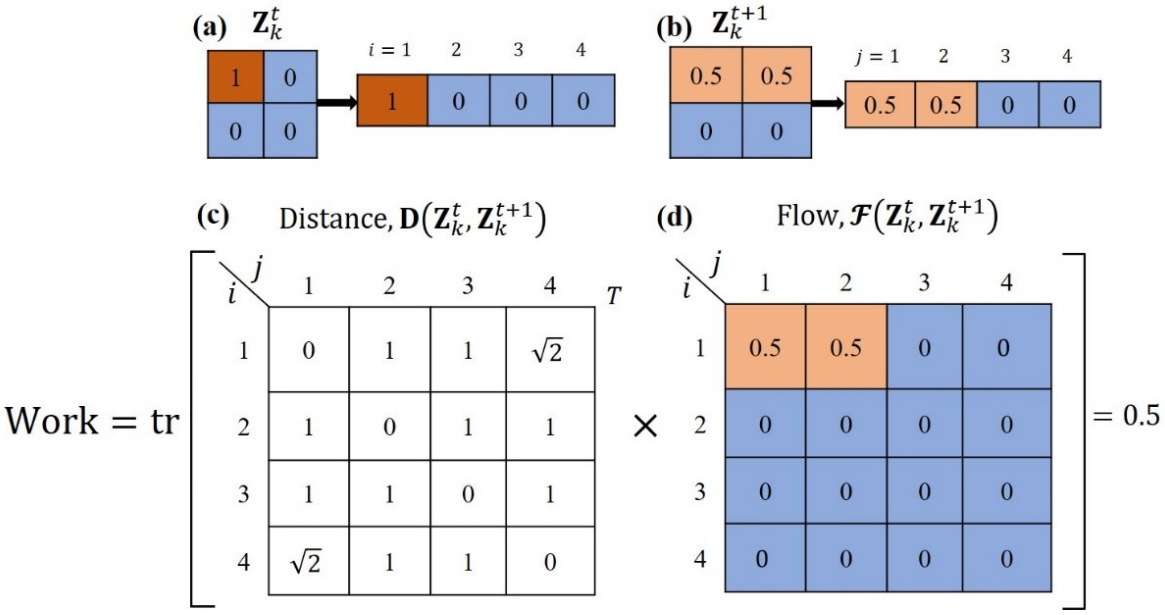

Figure 3: Visualization of numerical example for computation of work.

The MTM is determined by the *optimal* flow from $\mathbf{Z}_k^t$ to $\mathbf{Z}_k^{t+1}$ with the minimum work required to match between the two normalized melt pools/HAZs, which can be obtained by solving the optimization problem as illustrated in Table 2.

Table 2: Formulation for optimal flow from $\mathbf{Z}_k^t$ to $\mathbf{Z}_k^{t+1}$

$$\mathrm{MTM}_k^{t,t+1} = \min_{\mathcal{F}(\mathbf{Z}_k^t, \mathbf{Z}_k^{t+1})} \mathrm{Work}\left(\mathcal{F}(\mathbf{Z}_k^t, \mathbf{Z}_k^{t+1})\right)$$

Subject to

Non-negativity	$\not{f}_{ij}^{t,t+1} \geq 0 \quad \forall i = 1, \dots, rc; \ \forall j = 1, \dots, rc$	(6)
Upper bounds of flow	$\sum_{i=1}^{rc} \not{f}_{ij}^{t,t+1} = w_{k,j}^{t+1} \quad \forall j = 1, \dots, rc$	(7)
	$\sum_{j=1}^{rc} \not{f}_{ij}^{t,t+1} = w_{k,i}^{t} \quad \forall i = 1, \dots, rc$	(8)

where the objective function is inspired by the Wasserstein distance, which is the minimum necessary work to transport weight from $\mathbf{Z}_k^t$ to match $\mathbf{Z}_k^{t+1}$. Equation (6) enforces non-negativity requirements to each entry in $\mathcal{F}(\mathbf{Z}_k^t, \mathbf{Z}_k^{t+1})$ (i.e., $\not{f}_{ij}^{t,t+1}$). Equation (7) and (8) specify the upper bounds of the total incoming and outgoing flow, respectively. More specifically, the constraint (7)

signifies that the total weight in $\mathbf{Z}_k^t$ matched to the j-th pixel in $\mathbf{Z}_k^{t+1}$ does not exceed $w_{k,j}^{t+1}$, and similarly the constraint (8) ensures that the total weight in $\mathbf{Z}_k^{t+1}$ matched from the i-th pixel in $\mathbf{Z}_k^t$ does not exceed $w_{k,i}^t$. The formulated MTM metric is based on the Wasserstein distance with equal weight distributions, and the weight flows from one distribution to match with the weight of another distribution.

The rationale of using the WD-based metric is firstly due to its great flexibility in accurately capturing the morphological dynamics in a series of melt pools and HAZs [59]. The extracted GTM and MTM features can be used to characterize the instantaneous change of melt pool and HAZ morphologies which are closely related to AM process stability. Furthermore, the extracted GTM and MTM features also demonstrate the rotation-invariant property, as shown below. This favorable property makes it possible to establish one benchmark distribution for all the layers with completely different printing trajectories.

Proposition: Both GTM and MTM are melt pool rotation-invariant metrics.

Proof: For a given pair of $(\mathbf{Z}_k^t, \mathbf{Z}_k^{t+1})$, denote the optimal solution of Table 2 as $\boldsymbol{\mathcal{F}}^*$. Consider the case that $(\mathbf{Z}_k^t, \mathbf{Z}_k^{t+1})$ rotates with an angle α, and denote it as $\left(\tilde{\mathbf{Z}}_k^t, \tilde{\mathbf{Z}}_k^{t+1}\right) = (\mathbf{Z}_k^t\mathbf{R}(\alpha), \mathbf{Z}_k^{t+1}\mathbf{R}(\alpha))$, where $\mathbf{R}(\alpha)$ is the rotation matrix. If MTM is melt pool rotation-variant, then $\boldsymbol{\mathcal{F}}^*$ will not be the optimal solution of Table 2 with the input $(\tilde{\mathbf{Z}}_k^t, \tilde{\mathbf{Z}}_k^{t+1})$. Assume the optimal solution is $\tilde{\boldsymbol{\mathcal{F}}}^*$, then we can have

$$\text{Work}\left(\tilde{\boldsymbol{\mathcal{F}}}^*\left(\tilde{\mathbf{Z}}_k^t, \tilde{\mathbf{Z}}_k^{t+1}\right)\right) < \text{Work}\left(\boldsymbol{\mathcal{F}}^*\left(\tilde{\mathbf{Z}}_k^t, \tilde{\mathbf{Z}}_k^{t+1}\right)\right) = \text{Work}\left(\boldsymbol{\mathcal{F}}^*(\mathbf{Z}_k^t\mathbf{R}(\alpha), \mathbf{Z}_k^{t+1}\mathbf{R}(\alpha))\right)$$

According to the *Definition V*, for a given flow $\boldsymbol{\mathcal{F}}$, $\boldsymbol{\mathcal{F}}(\mathbf{Z}_k^t\mathbf{R}(\alpha), \mathbf{Z}_k^{t+1}\mathbf{R}(\alpha)) = \boldsymbol{\mathcal{F}}(\mathbf{Z}_k^t, \mathbf{Z}_k^{t+1})$. Thus,

$$\text{Work}\left(\boldsymbol{\mathcal{F}}^*(\mathbf{Z}_k^t\mathbf{R}(\alpha), \mathbf{Z}_k^{t+1}\mathbf{R}(\alpha))\right) = \text{Work}\left(\boldsymbol{\mathcal{F}}^*(\mathbf{Z}_k^t, \mathbf{Z}_k^{t+1})\right) \leq \text{Work}\left(\tilde{\boldsymbol{\mathcal{F}}}^*\left(\tilde{\mathbf{Z}}_k^t, \tilde{\mathbf{Z}}_k^{t+1}\right)\right)$$

which indicates $\text{Work}\left(\widetilde{\boldsymbol{\mathcal{F}}}^*\left(\tilde{\mathbf{Z}}_k^t, \tilde{\mathbf{Z}}_k^{t+1}\right)\right) < \text{Work}\left(\widetilde{\boldsymbol{\mathcal{F}}}^*\left(\tilde{\mathbf{Z}}_k^t, \tilde{\mathbf{Z}}_k^{t+1}\right)\right)$. This, however, is impossible. Thus, based on the proof by contradiction, MTM is melt pool rotation-invariant.

Similar proof can be applied to GTM. This rotation-invariant property for the proposed GTM and MTM metrics ensures that layers with different major printing orientations can share the same benchmark for AM layer-wise certification.

To find the MTM feature values, the optimization problem in Table 2 can be solved effectively by an efficient numerical algorithm (i.e., Algorithm 2M) proposed in [60], which is a cascadic multilevel primal-dual based algorithm. In this algorithm, the WD metrics are iteratively updated, where the coarse grids are used as the initial solution for solving the problem using the finer grids. This iterative mechanism significantly reduces the computational time to find the optimal solution. More specifically, the normalized melt pools/HAZs, denoted as $\mathbf{Z}_k^t$ and $\mathbf{Z}_k^{t+1}$ in Table 2, are corresponding to two distributions between which to calculate the WD metrics in [60], and the feature $\text{MTM}_k^{t,t+1}$ in our problem is corresponding to the optimal transport between $\mathbf{Z}_k^t$ and $\mathbf{Z}_k^{t+1}$. Once defining the initiation parameters including grid step size, number of grid levels, and the sequence of stopping tolerance, the optimal solution is computed following an iterative approach with different sizes of the grids. The computational cost of this algorithm in the proposed framework will be examined in the case study (Sec. 4).

3.3 Layer-wise Feature Extraction for Process Anomaly Detection

Based on the new transition metrics developed, the layer-wise features can be extracted. Since the transition metrics characterize the morphological dynamics of the melt pools and HAZs, their values should be very small when the AM process is healthy, and relatively large when there is a process anomaly. As a result, the maximum values of both features are used to quantify the morphology series' most extreme change for layer-wise anomaly detection. This is similar to the

idea of using group control chart in statistical quality control in order to control the type I error rate when simultaneously monitoring multiple data streams [61], [62]. Therefore, the maximum of all the $\mathrm{GTM}(\mathbf{X}_k^t, \mathbf{X}_k^{t+1})$ values is captured from each layer, and thus the relevant layer-wise feature $\ell\mathrm{GTM}_l^k$ can be calculated in Equation (9),

$$\ell\mathrm{GTM}_l^k = \max_{t\in\mathcal{T}_l}\{\mathrm{GTM}(\mathbf{X}_k^t, \mathbf{X}_k^{t+1})\} \quad (k = 1,2) \tag{9}$$

where $\mathcal{T}_l$ represents the set of time stamps within the build of the l-th layer.

In addition, the layer-wise melt pools/HAZs morphological dynamics can be characterized by the maximum of the multiple MTM values extracted from the consecutive melt pools/HAZs in the same layer, denoted as $\ell\mathrm{MTM}_l^k$, as calculated in Equation (10),

$$\ell\mathrm{MTM}_l^k = \max_{t\in\mathcal{T}_l}\left\{\mathrm{MTM}_k^{t,t+1}\right\} \quad (k = 1,2) \tag{10}$$

where $\mathcal{T}_l$ represents the set of time stamps that are within the build of the l-th layer.

3.4 *In-situ* Layer-wise Anomaly Detection based on Supervised Learning

Supervised learning algorithms can be used to establish a distinction between healthy and unhealthy layers based on the layer-wise features extracted. The post-manufacturing XCT scanning can be used to obtain structural quality information of each layer, providing the ground truth information to the data set. For layer-wise anomaly detection, one layer is labeled as abnormal if there is at least one porosity observed. It's worth noting that all different machine learning methods can be used to detect layer-wise anomalies. The support vector machine (SVM) technique is adopted in this work, because of the flexibility it can offer in learning the decision boundaries by varying kernel functions. The SVM classifier can be trained by finding the hyperplane that best separates all data points of distinct classes using a training data set with labeling information, and the complexity of the hyperplane can be determined through cross validation [63]. In summary, the newly proposed *in-situ* layer-wise anomaly detection algorithm is illustrated in Table 3.

Table 3: The proposed algorithm for *in-situ* layer-wise anomaly detection for DED processes.

Input: Layer-wise original thermal images $\{\mathbf{I}^t \in \mathbb{R}^{r\times c}\}$, where $t \in \mathcal{T}_l$, and $\mathcal{T}_l$ represents the set of time stamps that are within the build of the l-th layer.
Output: *In-situ* layer-wise anomaly detection.

Algorithm:
Step 1 (Melt pool & HAZ identification):
1.1: Rotate original thermal images as $\mathbf{X}^t(\theta) \in \mathbb{R}^{r\times c}$ based on the Equation (1).
1.2: Generate melt pools/HAZs by segmenting $\mathbf{X}^t(\theta)$ as $\mathbf{X}_k^t \in \mathbb{R}^{r\times c}$ by using Equation (2) ($k = 1,2$).
Step 2 (Melt pool & HAZ transition metrics calculation):
2.1: Calculate the $\mathrm{GTM}\left(\mathbf{X}_k^t, \mathbf{X}_k^{t+1}\right)$ values based on Equation (3).
2.2: Calculate the $\mathrm{MTM}_k^{t,t+1}$ values by solving the optimization problem in Table 2.
Step 3 (Layer-wise feature extraction):
3.1: Compute the $\ell\mathrm{GTM}_l^k$ value using the Equation (9).
3.2: Compute the $\ell\mathrm{MTM}_l^k$ value using Equation (10).
Step 4 (Supervised learning for *in-situ* layer-wise anomaly detection):
4.1: Train the SVM model using $\ell\mathrm{GTM}_l^k$, $\ell\mathrm{MTM}_l^k$ ($k = 1,2$) and layer-wise binary response variable of training dataset.
4.2: Assess the average performance of the model based on the test data set.

4. Case Study

In this section, the proposed *in-situ* layer-wise anomaly detection method is validated based on the data collected from two specimens using the DED process, which is one of the most common techniques to perform powder-based DED.

4.1 Experimental Setup

The machine used for data collection was the LENS 750 machine manufactured by OPTOMEC, and the machine is equipped with the 1kW Nd:YAG laser [16]. To evaluate the robustness of the proposed method, two specimens with different geometries (i.e., one thin wall and one cylindrical shaped part) were fabricated using the Ti–6Al–4V powder as the feedstock material. The process parameters used for both specimen fabrication are listed in Table 4 [16].

Table 4: Process parameters for fabricating the specimens.

Parameters	Thin wall	Cylinder
Scan speed	30 inch/min	40 inch/min
Powder feed rate	4 rpm	3 rpm
Hatch spacing	0.02 inch	0.02 inch
Power	300 W	300 W
Layer thickness	0.02 inch	0.015 inch
Nozzle diameter	0.035 inch	0.035 inch
Number of thermal images captured	1557	2827
Number of layers	60	69
Number of abnormal layers	26	58
Infill pattern	-	Unidirectional (180° rotation between layers)

For process data collection, the dual-wavelength coaxial pyrometer (Stratonics, Inc.) captures the temperature distribution from the top view of melt pool. The key benefit of using the pyrometer camera is that the image data collected demonstrate reduced motion blur, as it has a specific exposure period (2.0274 ms) with the nominal image collection rate of approximately 6.4 Hz. A brief sketch of the experimental setup with the sensor positioning is illustrated in Figure 4.

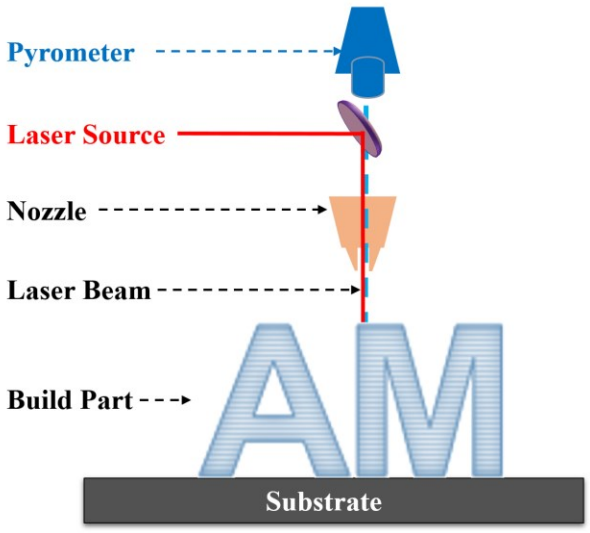

Figure 4: Experimental Setup.

Each observed thermal image is in the form of a 752×480 matrix, which consists of the temperature values at each pixel within the range of 1000-2500 °C. During the thin wall fabrication, the captured melt pools in each layer represent identical orientation, due to its unidirectional printing path. However, for the cylindrical specimen, the layer-wise melt pools demonstrate varying orientations due to the complex printing paths. Furthermore, using the XCT inspection (Skyscan 1172) technology, the porosities in the printed specimens were characterized, and thus the layer-wise process data were labeled using the porosity characterization results [14]. All the layers that include at least one pore with diameter larger than 0.05 mm were labeled as unhealthy [3].

4.2 Benchmark Method Selection

Two benchmark methods of layer-wise AM process anomaly detection are selected to compare with the proposed method. The first benchmark method was the layer-wise anomaly detection model proposed by Seifi *et al.* [3], which leveraged multi-linear principal component analysis (MPCA). In this approach, the MPCA algorithm was used for dimensionality reduction for each single thermal image, and then the volume of the convex hull formed by the extracted MPCs from each layer was employed as a layer-wise process feature for anomaly detection. In addition, the maximum norm value of the residual from the MPCA modeling within a layer was used as a secondary layer-wise feature during classification for anomaly detection. The effectiveness of this benchmark method was validated by comparing with the traditional machine learning driven anomaly detection approaches.

More recently, *in-situ* layer-wise certification of Direct Laser Deposition (DLD) process based on image series analysis was proposed by Esfahani *et al.* [16]. This method leverages the image registration technique to characterize the thermal history dynamics in the layer-wise thermal

images. Moreover, the Gaussian process (GP) models were employed to characterize the unexplained variation component by the image registration operation. The effectiveness of this benchmark method was validated by comparing with the approach proposed by Seifi *et al.* [4].

4.3 Results and Discussions

In this study, to compare the effectiveness of the proposed and the benchmark methods, both thin wall and cylinder data set were randomly split into the training layer set (80%) and testing layer set (20%), and 200 replications of this evaluation were performed to assess the average performance. Basically, using the training layer set the Gaussian SVM classification model can be trained when the GTM and MTM features have been defined, which can then be used to predict the labels of newly observed layers. Specifically, the classifier is fed a vector of response labels (0 for healthy, 1 for unhealthy) and a matrix of four predictors: the GTM and MTM extracted from the melt pool and tail region, respectively. The features of GTM and MTM are associated with the segmented melt pools/HAZs of thermal images, and the selection of temperature range of interests to segment the HAZ affects the extracted features and the prediction accuracy. In this case, the melt pool regions were segmented based on the melting point of the feedstock material and above, i.e., $\mathcal{R}_1 = [1636, +\infty)$, and the HAZs were segmented considering some specific temperature to the melting point of the feedstock material, i.e., $\mathcal{R}_2 = [T_0, 1636)$, which can define as the tail region of the melt pool.

The lower bound T_0 of the tail region temperature range can be considered as the tuning parameter in the proposed approach. By tuning the value of T_0, the effect of different temperature ranges of interests on the extracted features in both the thin wall and cylindrical specimen can be depicted as shown in the Figure 5. It can be observed that different values of T_0 lead to different

distinguishability between the healthy and unhealthy layers for both specimens, demonstrating the necessity of parameter tuning for the lower bound temperature T_0.

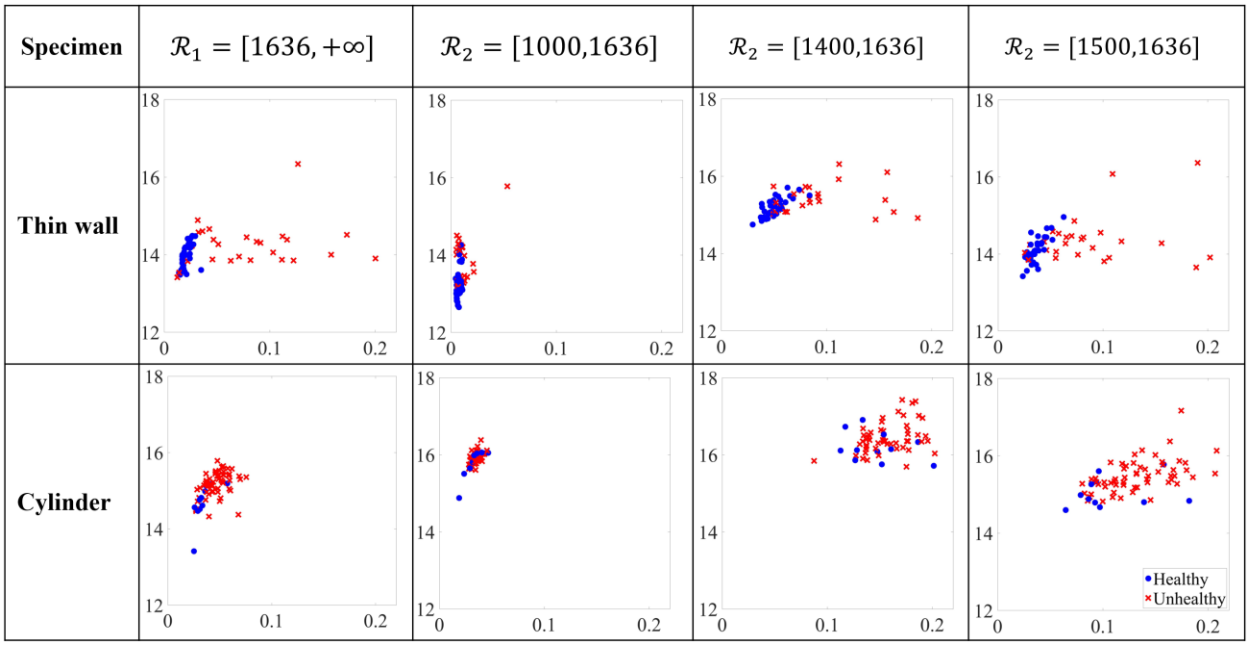

Figure 5: Extracted layer-wise features of ℓGTM (x-axis) vs ℓMTM (y-axis) for different temperature ranges of interest, where blue circles denote healthy layers and red crosses denote unhealthy layers.

Four key performance metrics (i.e., accuracy, recall, precision, and Fscore) are used to evaluate both methods given the same data set. The four metrics are commonly used in evaluating supervised learning methods [4], [13], [16], and are defined as below.

$$\text{Accuracy} = \frac{\text{TP+TN}}{\text{TP+FP+TN+FN}} \tag{11}$$

$$\text{Recall} = \frac{\text{TP}}{\text{TP+FN}} \tag{12}$$

$$\text{Precision} = \frac{\text{TP}}{\text{TP+FP}} \tag{13}$$

$$\text{Fscore} = 2 \times \frac{\text{Precision} \times \text{Recall}}{\text{Precision+Recall}} \tag{14}$$

where TP, TN, FN, and FP denote True-Positive, True-Negative, False-Negative and False-Positive, respectively, which are the key elements in confusion matrix. More specifically, True-Positive (TP) denotes accurate prediction of unhealthy layers, whereas True-Negative (TN) represents the layers accurately predicted as healthy. In addition, False-Negative (FN) denotes the

unhealthy layers predicted inaccurately as healthy, while False-Positive (FP) represents the inaccurate prediction of healthy layers as unhealthy. Moreover, the Fscore represents the harmonic mean of precision and recall, which is used in this paper as the key indicator for performance comparison.

As mentioned above the tuning parameter affects the extracted features and subsequently the prediction results. Therefore, by tuning the temperature range of the tail region, the performance metrics are listed as shown in the Table 5, where $\mathcal{R}_1$ is always fixed and $\mathcal{R}_2$ changes as the T_0 value is tuned. From Table 5, it is observed that in the case of thin wall, $T_0 = 1000℃$ (bolded) provides the highest Fscore value. Furthermore, in the case of cylinder, the Fscore value shows the best results when $T_0 = 1400℃$ (bolded).

Table 5: Performance comparison by tuning temperature range of interest ($\mathcal{R}_2$).

Specimen	Metric	T_0					
		1000℃	1100℃	1200℃	1300℃	1400℃	1500℃
Thin wall	Accuracy	**96.00%**	95.95%	96.65%	94.45%	88.35%	92.95%
	Precision	**96.80%**	97.70%	97.35%	92.42%	87.96%	98.03%
	Recall	**99.82%**	93.77%	94.04%	95.64%	89.37%	86.11%
	F-score	**96.04%**	95.10%	94.85%	93.18%	87.42%	90.33%
Cylinder	Accuracy	84.73%	84.09%	80.73%	83.00%	**86.05%**	83.00%
	Precision	82.50%	84.27%	81.55%	81.68%	**83.27%**	82.24%
	Recall	97.91%	97.88%	96.83%	99.81%	**100.00%**	98.31%
	F-score	90.07%	90.27%	88.13%	89.52%	**90.67%**	89.23%

The performance metrics of the proposed and benchmark methods are summarized in Table 6. Furthermore, a number of sample size values were explored to examine the effects of the sample size used in fitting the GP model for the error matrix in Esfahani *et al.* [16] for a fair comparison. When comparing the Fscore, it is observed that the proposed method outperforms both benchmark methods for the thin wall specimen. Moreover, for the cylindrical specimen, the proposed method outperforms Seifi *et al.* [4] in all four metrics, and demonstrates comparable (or slightly better)

Fscore results with Esfahani *et al.* [16]. The good performance of the proposed method is mainly due to its joint consideration of the layer-wise melt pools/HAZs morphological dynamics. In addition, given the robustness in the performance of the proposed method in both thin wall and cylindrical specimens, the proposed method can be applied for *in-situ* layer-wise anomaly detection for intricate shaped parts.

Table 6: Performance comparison summary.

Specimen	Metric	Proposed Method	Seifi *et al.* [4]	Esfahani *et al.* [16]					
				s=50	s=100	s=150	s=200	s=300	s=400
Thin wall	Accuracy	**96.38%**	94.67%	93.54%	93.17%	93.00%	93.92%	93.12%	93.25%
	Precision	**97.36%**	95.91%	94.75%	91.88%	91.63%	93.64%	91.85%	92.50%
	Recall	**94.47%**	90.98%	91.20%	93.58%	93.58%	93.68%	93.68%	93.58%
	F-score	**95.34%**	93.24%	92.36%	92.10%	91.97%	93.06%	92.10%	92.38%
Cylinder	Accuracy	**85.07%**	73.60%	84.29%	84.21%	83.96%	83.93%	83.11%	83.21%
	Precision	**84.71%**	81.46%	84.97%	84.96%	84.86%	84.85%	84.76%	84.78%
	Recall	**100.00%**	88.05%	99.18%	98.94%	98.72%	98.68%	97.76%	97.89%
	F-score	**91.56%**	84.12%	91.26%	91.18%	91.02%	91.00%	90.52%	90.59%

There are three possible reasons for the classification errors observed in the case study. Firstly, the discrete data sampling of the pyrometer camera may potentially lead to a lot of missing data in the thermal data collection, resulting in missing defect inducing process information. Second, the characterization of XCT scanning may be subject to noise and error, leading to occasional labeling errors in the data set. Third, the proposed *in-situ* layer-wise anomaly detection approach ignores the impacts of re-melting between consecutive layers and adjacent tracks, which may eliminate some porosities formed in the preceding layer/track during subsequent layer/track deposition.

The average computational efficiency of the proposed method is illustrated in Figure 6, where the average computation time and the average build time for each layer is compared for both specimens. The processor used to implement the proposed method was Intel® Core™ Processor i7-7700 CPU @ 3.60GHz. It is worth noting that the average computation for the proposed method takes significantly shorter time than its corresponding layer-wise build time for both thin wall and

cylinder specimen. As a result, the proposed method can facilitate layer-wise AM certification in real time, potentially enabling real-time process control for quality improvement.

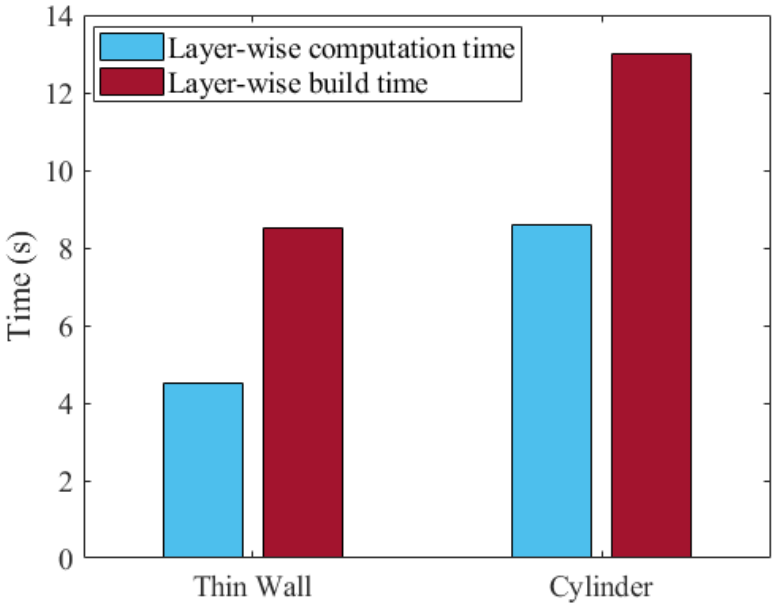

Figure 6: Layer-wise average computation time of the proposed method.

5. Conclusion and Future Work

The quality issues are the major barriers for wider and sustainable industrial adoption of the AM technology, and there is a need of reliable techniques to detect quality issues (i.e., porosity, mini cracks, lack of fusion, etc.) in AM processes. Different approaches like FEMs are used to characterize the anomaly based on thermomechanical relationship, but they cannot realistically capture process uncertainty. These limitations are addressed by the data-driven approaches where usually the individual thermal images of the melt pools are used for local anomaly prediction. Few approaches are proposed for layer-wise anomaly detection, and the extracted features cannot explicitly characterize melt pool/HAZ morphological dynamics.

This paper proposes a novel formulation of melt pools and HAZs morphological dynamics through which the new melt pool/HAZ transition metrics are derived. Furthermore, novel layer-

wise process key features are derived from the characterization of melt pools/HAZ morphological dynamics for AM layer-wise anomaly detection. Specifically, morphological transition between consecutive melt pools/HAZs along with the global temperature shift are extracted as the novel features. Based on the extracted layer-wise features, the SVM classification approach is used for *in-situ* layer-wise anomaly detection. The specimens of a thin wall and a cylinder were fabricated using the DED process to validate the proposed methodology. The anomaly detection accuracy of the proposed model is reasonably high and outperforms both benchmark methods, which are both state-of-the-art AM layer-wise anomaly detection methods.

For future research, a couple of interesting topics remain open. First, the inter-layer and inter-track dependence during fabrication can be characterized to quantify the re-melting effect between the adjacent layers/tracks. Second, a part certification framework can be established to quantify the size and severity of the defects and their impact to the part functionality. Finally, layer-wise process control algorithms can be used in conjunction with the *in-situ* monitoring scheme to adjust process parameters for quality improvement of the AM parts.

Acknowledgments

This work was partially sponsored by the National Science Foundation (No. CMMI-2046515).

References

[1] N. Shamsaei, A. Yadollahi, L. Bian, and S. M. Thompson, "An overview of Direct Laser Deposition for additive manufacturing; Part II: Mechanical behavior, process parameter optimization and control," *Addit. Manuf.*, vol. 8, pp. 12–35, 2015, doi: 10.1016/j.addma.2015.07.002.

[2] C. Liu, W. Tian, and C. Kan, "When AI meets additive manufacturing: Challenges and emerging opportunities for human-centered products development," *J. Manuf. Syst.*, 2022.

[3] Q. Tian, S. Guo, E. Melder, L. Bian, and W. Guo, "Deep Learning-based Data Fusion Method for In-Situ Porosity Detection in Laser-based Additive Manufacturing," *J. Manuf. Sci. Eng.*, vol. 143, no. April, pp. 1–38, 2020, doi: 10.1115/1.4048957.

[4] S. H. Seifi, W. Tian, H. Doude, M. A. Tschopp, and L. Bian, "Layer-Wise Modeling and Anomaly Detection for Laser-Based Additive Manufacturing," *J. Manuf. Sci. Eng. Trans. ASME*, vol. 141, no. 8, pp. 1–12, 2019, doi: 10.1115/1.4043898.

[5] K. Jurrens and Energetics Incorporated, "Measurement Science Roadmap for Metal-Based Additive Manufacturing," *Addit. Manuf.*, p. 86, 2013.

[6] C.-J. Bae, A. B. Diggs, and A. Ramachandran, "Quantification and certification of additive manufacturing materials and processes," in *Additive Manufacturing*, Elsevier, 2018, pp. 181–213.

[7] Z. Chen, C. Han, M. Gao, S. Y. Kandukuri, and K. Zhou, "A review on qualification and certification for metal additive manufacturing," *Virtual Phys. Prototyp.*, vol. 17, no. 2, pp. 382–405, 2022, doi: 10.1080/17452759.2021.2018938.

[8] AIA, "Report: Recommended Guidance for Certification of AM Components." pp. 0–39, 2020.

[9] L. R. & T. Ltd, "Guidance Notes for Additive Manufacturing of Metallic Parts," *Additive Manufacturing*, no. January. 2020.

[10] J. Romano, L. Ladani, and M. Sadowski, "Thermal Modeling of Laser Based Additive Manufacturing Processes within Common Materials," *Procedia Manuf.*, vol. 1, pp. 238–250, 2015, doi: 10.1016/j.promfg.2015.09.012.

[11] H. Tian, X. Chen, Z. Yan, X. Zhi, Q. Yang, and Z. Yuan, "Finite-element simulation of melt pool geometry and dilution ratio during laser cladding," *Appl. Phys. A Mater. Sci. Process.*, vol. 125, no. 7, 2019, doi: 10.1007/s00339-019-2772-9.

[12] M. Khanzadeh, W. Tian, A. Yadollahi, H. R. Doude, M. A. Tschopp, and L. Bian, "Dual process monitoring of metal-based additive manufacturing using tensor decomposition of thermal image streams," *Addit. Manuf.*, vol. 23, no. July, pp. 443–456, 2018, doi: 10.1016/j.addma.2018.08.014.

[13] M. Khanzadeh, S. Chowdhury, M. Marufuzzaman, M. A. Tschopp, and L. Bian, "Porosity prediction: Supervised-learning of thermal history for direct laser deposition," *J. Manuf. Syst.*, vol. 47, no. April, pp. 69–82, 2018, doi: 10.1016/j.jmsy.2018.04.001.

[14] M. Khanzadeh, S. Chowdhury, M. A. Tschopp, H. R. Doude, M. Marufuzzaman, and L. Bian, "In-situ monitoring of melt pool images for porosity prediction in directed energy deposition processes," *IISE Trans.*, vol. 51, no. 5, pp. 437–455, 2019, doi: 10.1080/24725854.2017.1417656.

[15] M. Grasso, A. G. Demir, B. Previtali, and B. M. Colosimo, "In situ monitoring of selective laser melting of zinc powder via infrared imaging of the process plume," *Robot. Comput. Integr. Manuf.*, vol. 49, no. February 2017, pp. 229–239, 2018, doi: 10.1016/j.rcim.2017.07.001.

[16] M. N. Esfahani, M. Bappy, L. Bian, and W. Tian, "In-situ Layer-wise Certification for Direct Laser Deposition Processes based on Thermal Image Series Analysis," *J. Manuf.*

Process., 2022.

[17] L. Scime and J. Beuth, "Melt pool geometry and morphology variability for the Inconel 718 alloy in a laser powder bed fusion additive manufacturing process," *Addit. Manuf.*, vol. 29, no. May, p. 100830, 2019, doi: 10.1016/j.addma.2019.100830.

[18] C. Wang, X. P. Tan, S. B. Tor, and C. S. Lim, "Machine learning in additive manufacturing: State-of-the-art and perspectives," *Addit. Manuf.*, vol. 36, no. January, p. 101538, 2020, doi: 10.1016/j.addma.2020.101538.

[19] K. Naresh, K. A. Khan, R. Umer, and W. J. Cantwell, "The use of X-ray computed tomography for design and process modeling of aerospace composites: A review," *Mater. Des.*, vol. 190, p. 108553, 2020, doi: 10.1016/j.matdes.2020.108553.

[20] H. D. Vora and S. Sanyal, *A comprehensive review: metrology in additive manufacturing and 3D printing technology*, vol. 5, no. 4. Springer International Publishing, 2020.

[21] A. Haleem and M. Javaid, "Role of CT and MRI in the design and development of orthopaedic model using additive manufacturing," *J. Clin. Orthop. Trauma*, vol. 9, no. 3, pp. 213–217, 2018, doi: 10.1016/j.jcot.2018.07.002.

[22] C. Kim, H. Yin, A. Shmatok, B. C. Prorok, X. Lou, and K. H. Matlack, "Ultrasonic nondestructive evaluation of laser powder bed fusion 316L stainless steel," *Addit. Manuf.*, vol. 38, no. January, p. 101800, 2021, doi: 10.1016/j.addma.2020.101800.

[23] Z. Ye, C. Liu, W. Tian, and C. Kan, "In-situ point cloud fusion for layer-wise monitoring of additive manufacturing," *J. Manuf. Syst.*, vol. 61, pp. 210–222, 2021.

[24] C. Liu *et al.*, "Toward Online Layer-wise Surface Morphology Measurement in Additive Manufacturing Using a Deep Learning-based Approach," *J. Intell. Manuf.*

[25] J. Lifton and T. Liu, "An adaptive thresholding algorithm for porosity measurement of additively manufactured metal test samples via X-ray computed tomography," *Addit. Manuf.*, vol. 39, p. 101899, 2021, doi: 10.1016/j.addma.2021.101899.

[26] P. Pokorný, Š. Václav, J. Petru, and M. Kritikos, "Porosity analysis of additive manufactured parts using caq technology," *Materials (Basel).*, vol. 14, no. 5, pp. 1–14, 2021, doi: 10.3390/ma14051142.

[27] C. Gobert, A. Kudzal, J. Sietins, C. Mock, J. Sun, and B. McWilliams, "Porosity segmentation in X-ray computed tomography scans of metal additively manufactured specimens with machine learning," *Addit. Manuf.*, vol. 36, no. August 2019, p. 101460, 2020, doi: 10.1016/j.addma.2020.101460.

[28] F. Soltani, M. Goueygou, Z. Lafhaj, and B. Piwakowski, "Relationship between ultrasonic Rayleigh wave propagation and capillary porosity in cement paste with variable water content," *NDT E Int.*, vol. 54, pp. 75–83, 2013, doi: 10.1016/j.ndteint.2012.12.003.

[29] N. V. Karthik, H. Gu, D. Pal, T. Starr, and B. Stucker, "High frequency ultrasonic non destructive evaluation of additively manufactured components," *24th Int. SFF Symp. - An Addit. Manuf. Conf. SFF 2013*, pp. 311–325, 2013.

[30] M. Khanzadeh, M. Dantin, W. Tian, M. W. Priddy, H. Doude, and L. Bian, "Fast Prediction of Thermal Data Stream for Direct Laser Deposition Processes Using Network-

Based Tensor Regression," *J. Manuf. Sci. Eng. Trans. ASME*, vol. 144, no. 4, pp. 1–16, 2022, doi: 10.1115/1.4052207.

[31] Z. Xiyue, I. Aidin, K. Mojtaba, I. Farhad, and B. Linkan, "Automated Anomaly Detection of Laser-Based Additive Manufacturing Using Melt Pool Sparse Representation and Unsupervised Learning," *Solid Free. Fabr. 2018 Proc. 29th Annu. Int. Solid Free. Fabr. Symp. – An Addit. Manuf. Conf. Rev. Pap.*, pp. 376–387, 2021, doi: org/10.26153/tsw/17561.

[32] M. Mahmoudi, A. A. Ezzat, and A. Elwany, "Layerwise Anomaly Detection in Laser Powder-Bed Fusion Metal Additive Manufacturing," *J. Manuf. Sci. Eng. Trans. ASME*, vol. 141, no. 3, pp. 1–13, 2019, doi: 10.1115/1.4042108.

[33] M. Grasso and B. M. Colosimo, "Process defects and in situ monitoring methods in metal powder bed fusion: A review," *Meas. Sci. Technol.*, vol. 28, no. 4, pp. 1–40, 2017, doi: 10.1088/1361-6501/aa5c4f.

[34] J. A. Mitchell, T. A. Ivanoff, D. Dagel, J. D. Madison, and B. Jared, "Linking pyrometry to porosity in additively manufactured metals," *Addit. Manuf.*, vol. 31, no. July 2019, 2020, doi: 10.1016/j.addma.2019.100946.

[35] L. Scime and J. Beuth, "A multi-scale convolutional neural network for autonomous anomaly detection and classification in a laser powder bed fusion additive manufacturing process," *Addit. Manuf.*, vol. 24, no. October, pp. 273–286, 2018, doi: 10.1016/j.addma.2018.09.034.

[36] W. "Grace" Guo, Q. Tian, S. Guo, and Y. Guo, "A physics-driven deep learning model for process-porosity causal relationship and porosity prediction with interpretability in laser metal deposition," *CIRP Ann.*, vol. 69, no. 1, pp. 205–208, 2020, doi: 10.1016/j.cirp.2020.04.049.

[37] R. Reisch, T. Hauser, B. Lutz, M. Pantano, T. Kamps, and A. Knoll, "Distance-Based Multivariate Anomaly Detection in Wire Arc Additive Manufacturing," *Proc. - 19th IEEE Int. Conf. Mach. Learn. Appl. ICMLA 2020*, pp. 659–664, 2020, doi: 10.1109/ICMLA51294.2020.00109.

[38] C. Liu, A. C. C. Law, D. Roberson, and Z. (James) Kong, "Image analysis-based closed loop quality control for additive manufacturing with fused filament fabrication," *J. Manuf. Syst.*, vol. 51, no. April, pp. 75–86, 2019, doi: 10.1016/j.jmsy.2019.04.002.

[39] A. Al Mamun, C. Liu, C. Kan, and W. Tian, "Securing Cyber-Physical Additive Manufacturing Systems by In-situ Process Authentication using Streamline Video Analysis," *J. Manuf. Syst.*, 2022.

[40] C. Liu, Z. Kong, S. Babu, C. Joslin, and J. Ferguson, "An integrated manifold learning approach for high-dimensional data feature extractions and its applications to online process monitoring of additive manufacturing," *IISE Trans.*, vol. 53, no. 11, pp. 1215–1230, 2021.

[41] H. Yan, M. Grasso, K. Paynabar, and B. M. Colosimo, "Real-time Detection of Clustered Events in Video-imaging data with Applications to Additive Manufacturing," pp. 1–40, 2020.

[42] B. M. Colosimo and M. Grasso, “Spatially weighted PCA for monitoring video image data with application to additive manufacturing,” *J. Qual. Technol.*, vol. 50, no. 4, pp. 391–417, 2018, doi: 10.1080/00224065.2018.1507563.

[43] L. Chen, X. Yao, P. Xu, S. K. Moon, and G. Bi, “Rapid surface defect identification for additive manufacturing with in-situ point cloud processing and machine learning,” *Virtual Phys. Prototyp.*, vol. 16, no. 1, pp. 50–67, 2021, doi: 10.1080/17452759.2020.1832695.

[44] R. Li, M. Jin, and V. C. Paquit, “Geometrical defect detection for additive manufacturing with machine learning models,” *Mater. Des.*, vol. 206, p. 109726, 2021, doi: 10.1016/j.matdes.2021.109726.

[45] M. S. Tootooni, A. Dsouza, R. Donovan, P. K. Rao, Z. J. Kong, and P. Borgesen, “Classifying the Dimensional Variation in Additive Manufactured Parts from Laser-Scanned Three-Dimensional Point Cloud Data Using Machine Learning Approaches,” *J. Manuf. Sci. Eng. Trans. ASME*, vol. 139, no. 9, pp. 1–14, 2017, doi: 10.1115/1.4036641.

[46] A. Jaklič, M. Erič, I. Mihajlović, Ž. Stopinšek, and F. Solina, “Volumetric models from 3D point clouds: The case study of sarcophagi cargo from a 2nd/3rd century AD Roman shipwreck near Sutivan on island Brač, Croatia,” *J. Archaeol. Sci.*, vol. 62, pp. 143–152, 2015, doi: 10.1016/j.jas.2015.08.007.

[47] B. Yuan, B. Giera, G. Guss, M. Matthews, and S. McMains, “Semi-supervised convolutional neural networks for in-situ video monitoring of selective laser melting,” *Proc. - 2019 IEEE Winter Conf. Appl. Comput. Vision, WACV 2019*, pp. 744–753, 2019, doi: 10.1109/WACV.2019.00084.

[48] J. Francis and L. Bian, “Deep Learning for Distortion Prediction in Laser-Based Additive Manufacturing using Big Data,” *Manuf. Lett.*, vol. 20, pp. 10–14, 2019, doi: 10.1016/j.mfglet.2019.02.001.

[49] S. H. Seifi, A. Yadollahi, W. Tian, H. Doude, V. H. Hammond, and L. Bian, “In Situ Nondestructive Fatigue-Life Prediction of Additive Manufactured Parts by Establishing a Process–Defect–Property Relationship,” *Adv. Intell. Syst.*, p. 2000268, 2021.

[50] Q. Tian, S. Guo, E. Melder, L. Bian, and W. Guo, “Deep learning-based data fusion method for in situ porosity detection in laser-based additive manufacturing,” *J. Manuf. Sci. Eng. Trans. ASME*, vol. 143, no. 4, pp. 1–14, 2021, doi: 10.1115/1.4048957.

[51] D. Ye, J. Y. Hsi Fuh, Y. Zhang, G. S. Hong, and K. Zhu, “In situ monitoring of selective laser melting using plume and spatter signatures by deep belief networks,” *ISA Trans.*, vol. 81, no. May, pp. 96–104, 2018, doi: 10.1016/j.isatra.2018.07.021.

[52] Z. Yang, Y. Lu, H. Yeung, and S. Krishnamurty, “Investigation of deep learning for real-time melt pool classification in additive manufacturing,” in *2019 IEEE 15th international conference on automation science and engineering (CASE)*, 2019, pp. 640–647.

[53] W. Feng *et al.*, “Online defect detection method and system based on similarity of the temperature field in the melt pool,” *Addit. Manuf.*, vol. 54, p. 102760, 2022.

[54] Z. Shi, A. Al Mamun, C. Kan, W. Tian, and C. Liu, “An LSTM-Autoencoder Based Online Side Channel Monitoring Approach for Cyber-Physical Attack Detection in Additive Manufacturing,” *J. Intell. Manuf.*, 2021.

[55] Z. Shi, S. Mandal, S. Harimkar, and C. Liu, “Surface Morphology Analysis Using Convolutional Autoencoder in Additive Manufacturing with Laser Engineered Net Shaping,” *Procedia Manuf.*, vol. 53, pp. 16–23, 2021.

[56] H. Gaja and F. Liou, “Defect classification of laser metal deposition using logistic regression and artificial neural networks for pattern recognition,” *Int. J. Adv. Manuf. Technol.*, vol. 94, no. 1–4, pp. 315–326, 2018, doi: 10.1007/s00170-017-0878-9.

[57] F. Imani, A. Gaikwad, M. Montazeri, P. Rao, H. Yang, and E. Reutzel, “Process mapping and in-process monitoring of porosity in laser powder bed fusion using layerwise optical imaging,” *J. Manuf. Sci. Eng. Trans. ASME*, vol. 140, no. 10, 2018, doi: 10.1115/1.4040615.

[58] A. I. García-Moreno, J. M. Alvarado-Orozco, J. Ibarra-Medina, and E. Martínez-Franco, “Image-based porosity classification in Al-alloys by laser metal deposition using random forests,” *Int. J. Adv. Manuf. Technol.*, vol. 110, no. 9–10, pp. 2827–2845, 2020, doi: 10.1007/s00170-020-05887-6.

[59] W. Lee, W. Li, B. Lin, and A. Monod, “Tropical optimal transport and Wasserstein distances,” *Inf. Geom.*, pp. 1–13, 2021, doi: 10.1007/s41884-021-00046-6.

[60] J. Liu, W. Yin, W. Li, and Y. T. Chow, “Multilevel optimal transport: A fast approximation of wasserstein-1 distances,” *arXiv*, 2018.

[61] W. Tian, R. Jin, T. Huang, and J. A. Camelio, “Statistical process control for multistage processes with non-repeating cyclic profiles,” *IISE Trans.*, vol. 49, no. 3, pp. 320–331, 2017.

[62] L. Xiang and F. Tsung, “Statistical monitoring of multi-stage processes based on engineering models,” *IIE Trans.*, vol. 40, no. 10, pp. 957–970, 2008.

[63] J. Friedman, T. Hastie, and R. Tibshirani, *The elements of statistical learning. New York, NY, USA: Springer New York Inc.* 2001.

List of Figures

List of Tables